INL/CON-05-00568
PREPRINT

Influence Of Fluid-Property Variation On Turbulent Convective Heat Transfer In Vertical Annular Channel FLows

NURETH-11

Donald M. McEligot
Joong Hun Bae
Jung Yul Yoo
Haecheon Choi

October 2005

The INL is a
U.S. Department of Energy
National Laboratory
operated by
Battelle Energy Alliance

The 11th International Topical Meeting on Nuclear Thermal-Hydraulics (NURETH-11)
Popes' Palace Conference Center, Avignon, France, October 2-6, 2005

Paper: 018

INFLUENCE OF FLUID-PROPERTY VARIATION ON TURBULENT CONVECTIVE HEAT TRANSFER IN VERTICAL ANNULAR CHANNEL FLOWS

Joong Hun Bae, Jung Yul Yoo[1], Haecheon Choi[2]
School of Mechanical and Aerospace Engineering, Seoul National University
Seoul 151-744, Korea
jhbae@eddy.snu.ac.kr, jyyoo@snu.ac.kr, choi@socrates.snu.ac.kr

Donald M. McEligot
Idaho National Laboratory (INL), Idaho Falls, Idaho 83415-3885 USA
dm6@inel.gov

ABSTRACT

Influence of strongly-varying properties of supercritical-pressure fluids on turbulent convective heat transfer is investigated using direct numerical simulation. We consider thermally-developing upward flows in a vertical annular channel where the inner wall is heated with a constant heat flux and the outer wall is insulated. CO_2 is chosen as the working fluid at a pressure of 8 MPa, and the inlet Reynolds number based on the channel hydraulic diameter and the bulk velocity is $Re_0 = 8900$. It is shown that turbulent convective heat transfer characteristics of supercritical flow are significantly different from those of constant-property flow mainly due to spatial and temporal variations of fluid density. Non-uniform density distribution causes fluid particles to be accelerated either by expansion or buoyancy force near the heated wall, while temporal density fluctuations change the transport characteristics of turbulent heat and momentum via the buoyancy production terms arising from the correlations such as $\overline{\rho' u_x'}$, $\overline{\rho' u_r'}$ and $\overline{\rho' h'}$. Among various turbulence statistics, the streamwise turbulent heat flux shows a very peculiar transitional behavior due to the buoyancy effect, changing both in sign and magnitude. Consequently, a non-monotonic temperature distribution is developed in the flow direction, causing severe impairment of heat transfer in supercritical flows.

KEYWORDS

Supercritical fluid, Direct numerical simulation, Heat transfer, Buoyancy effect

1 INTRODUCTION

If a pure substance at a pressure greater than the critical pressure is heated from its subcooled state to a temperature above the critical temperature in a constant-pressure process, there will never be two phases present, and an equilibrium phase change from saturated liquid to saturated vapor will never exist. Rather, there will be a continuous change in density and at all times there will be only one phase present. The question then arises as to when do we have a liquid and when do we have a vapor? The answer is that this is not a valid question at supercritical pressure. Instead, we simply term the substance as a *fluid* or more precisely a *supercritical-pressure fluid*. However, rather arbitrarily, at temperatures below the critical temperature we may refer to it as a compressed liquid and at temperatures above the critical temperature as a superheated vapor. It should be emphasized, however, that at pressure above the critical pressure we never have a liquid and vapor phase of a pure substance existing in equilibrium (Sonntag & Van Wylen, 1981). Unlike the subcritical-pressure fluids, the fluid at supercritical pressure shows a

[1]Corresponding author, Tel: +82-2-880-7112, Fax:+82-2-883-0179

[2]also at National CRI Center for Turbulence and Flow Control Research, Institute of Advanced Machinery and Design, Seoul National University, Seoul 151-744, Korea

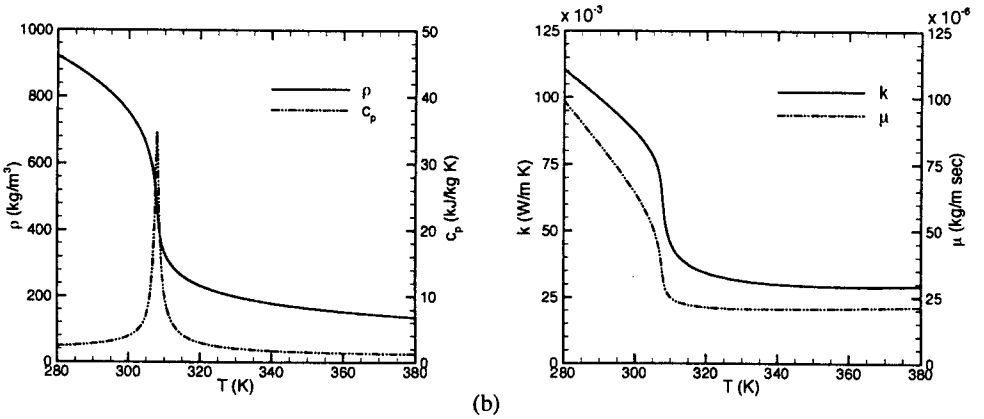

Figure 1: Thermo-physical property variation vs. temperature for supercritical-pressure carbon-dioxide (CO_2) at $P = 8$ MPa: (a) density ρ and specific heat at constant pressure c_p; (b) thermal conductivity k and dynamic viscosity μ.

very large property variation which occurs continuously when its characteristic changes from a liquid-like substance to a vapor-like one. This variation happens in a very narrow range of temperature across the pseudo-critical temperature (T_{pc}) at which c_p is the maximum. See Figure 1, for example, for the property variations in terms of temperature for supercritical-pressure CO_2 at a pressure of 8 MPa.

A large volume of experimental data accumulated in the past decades indicates that a serious heat transfer deterioration occurs in supercritical flows causing a significant rise in wall temperature. Sometimes, this deterioration occurs in forced convection with negligible buoyancy effect, which was particularly well ilustrated by the data of Shiralkar & Griffith (1970), or in other instances, it is frequently found in mixed convection under strong influence of buoyancy with such characteristics as a rapid rise in wall temperature causing localized sharp peaks in the wall temperature distribution (Shitsman (1963); Ackerman (1970); Fewster (1976); etc.). The former type of deterioration occurs at relatively high heat flux in relation to the mass flux and where the fluid temperature spans the pseudo-critical region in which the $T_b < T_{pc} < T_w$ condition is met. Flow orientation is not an essential factor in this case. However, in the latter case, flow orientation plays a very important role so that such a deterioration phenomenon only occurs in an upward flow in a vertical tube. In downward flows, however, an enhancement of heat transfer is observed (Fewster, 1976). Furthermore, this type of deterioration is not confined to the region of bulk temperature (T_b) in the viscinity of T_{pc} and can occur at all temperature ranges and even at subcritical pressure. More comprehensive reviews on the topic of heat transfer to supercritical-pressure fluids can be found in the articles by (Jackson & Hall, 1979a,b), and recently very extensive literature surveys on heat transfer and hydraulic resistance characteristics of supercritical-pressure fluids have been provided by Pioro *et al.* (2004a,b) and Duffey & Pioro (2005).

Many investigators tried to predict this peculiar characteristic of heat transfer to supercritical-pressure fluids with numerical methods using turbulence models. Until now, a lot of different turbulence models were tested (Koshizuka *et al.* (1995); He *et al.* (2004), etc.), but they were not always successful. Especially, He *et al.* (2004) performed a comparative study using a number of two-equation low-Reynolds-number turbulence models for mixed convection of supercritical-pressure CO_2 flows and found that the predicted performance varied significantly from model to model in terms of the buoyancy effect on heat transfer. They suggested that an improved turbulence model to treat the buoyancy effect is necessary. Unfortunately, the development of such a model is impeded by the lack of experimental data for detailed flow fields such as mean velocity and temperature distributions, turbulence statistics, etc. Advanced computational techniques such as direct numerical simulation (DNS) or large eddy simulation (LES) can be very useful alternatives to experiments if an accurate measurement of such data is extremely difficult to be achieved. But, such advanced numerical techniques are not readily available at the present time for this kind of problems. The present authors are among the first who successfully performed

DNS of supercritical CO_2 pipe flows with heat transfer (Bae *et al.* , 2003) and their research is now extended to more complex annular geometry. This situation is particularly relevant to the advancement of nuclear thermal hydraulics technology since the flow passages or the cooling channel geometries in many advanced concepts of nuclear reactor systems are composed of various types of sub-channels with complex, non-circular geometries (McEligot & Jackson (2004); McCreery *et al.* (2003); Cheng *et al.* (2003)). The studies of an annular flow with heat transfer from a heated inner rod may provide very useful information on heat transfer through boundary layers with convex curvature which is frequently found in many sub-channel geometries of advanced nuclear reactors. In the present paper we will discuss some of the interesting new results for supercritical annular channel flows with heat transfer.

2 GOVERNING EQUATIONS

In the present study, the low-Mach-number approximated Navier-Stokes equations (Pierce, 2001) are used as the governing equations for variable-property supercritical flows. Since these equations do not include the compressibility effect, all thermodynamic properties including density are treated as temperature-dependent properties at a constant thermodynamic pressure (P_0). The gravitational force term is included only in the axial momentum equation to account for the buoyancy effect without using the Bousinessq approximation.

- Continuity,

$$\frac{\partial \rho}{\partial t} + \frac{\partial (\rho u_j)}{\partial x_j} = 0; \tag{1}$$

- Momemtum,

$$\frac{\partial (\rho u_i)}{\partial t} + \frac{\partial (\rho u_i u_j)}{\partial x_j} = -\frac{\partial p}{\partial x_i} + \frac{\partial \tau_{ij}}{\partial x_j} - \frac{1}{Fr}\delta_{1i}\rho; \tag{2}$$

- Energy,

$$\frac{\partial (\rho h)}{\partial t} + \frac{\partial (\rho u_j h)}{\partial x_j} = -\frac{\partial q_j}{\partial x_j}; \tag{3}$$

where

$$\tau_{ij} = 2\frac{\mu}{Re}\left(S_{ij} - \frac{1}{3}\delta_{ij}\frac{\partial u_k}{\partial x_k}\right), \quad S_{ij} = \frac{1}{2}\left(\frac{\partial u_i}{\partial x_j} + \frac{\partial u_j}{\partial x_i}\right), \tag{4}$$

$$q_i = -\frac{k}{RePr}\frac{\partial T}{\partial x_i} = -\frac{1}{RePr}\frac{k}{c_p}\frac{\partial h}{\partial x_i}, \quad h = \frac{h^* - h_0}{c_{p0}T_0}. \tag{5}$$

These equations are nondimensionalized with inlet conditions (represented by subscript 0) and channel half width $\delta(= 0.5(r_o - r_i))$ and the non-dimensional parameters shown in the equations are defined as follows:

$$Re = \frac{\rho_0 U_0 \delta}{\mu_0}, \quad Pr = \frac{\mu_0 c_{p0}}{k_0}, \quad \frac{1}{Fr} = \frac{g\delta}{U_0^2} = \frac{1}{\beta_0 T_0}\frac{Gr^*}{Re^2}\frac{1}{Q^+}, \quad Gr^* = \frac{g\beta_0 q_w \delta^4}{\nu_0^2 k_0}, \quad Q^+ = \frac{q_w \delta}{k_0 T_0}. \tag{6}$$

Supercritical-pressure CO_2 is chosen as the working fluid at P_0 = 8 MPa, where P_0 is the inlet thermodynamic pressure which is assumed to be constant. The physical properties of CO_2 at supercritical pressure are obtained using PROPATH (PROPATH Group, 1999) which are provided by the International Association for the Properties of Water and Steam (IAPWS). These property data are tabulated in the following functional forms to be used in the main program.

$$T^* = T(P_0, h^*), \quad \rho^* = \rho(P_0, T^*), \quad \mu^* = \mu(P_0, T^*), \quad k^* = k(P_0, T^*), \quad c_p^* = c_p(P_0, T^*). \tag{7}$$

The reader may note that superscript * is used to denote the dimensional variables. These low-Mach-number Navier-Stokes equations are solved using a conservative space-time discretization method which was developed by Pierce (2001), Pierce & Moin (2004) and is also described well by Wall *et al.* (2002).

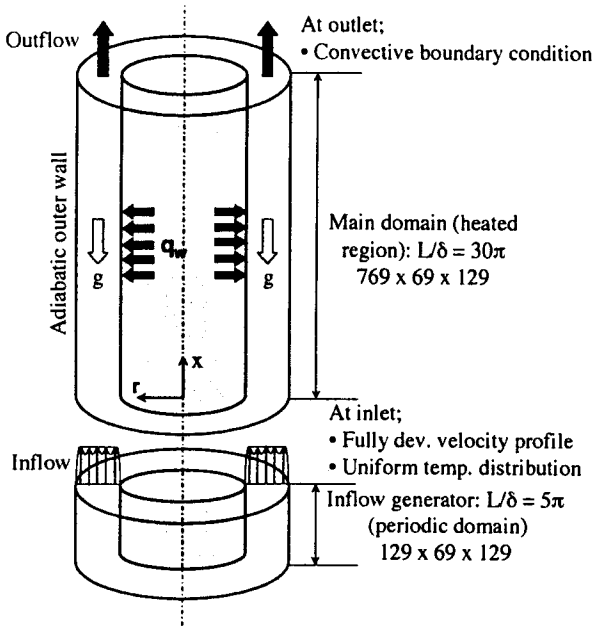

Figure 2: Schematic diagram of the flow region and boundary conditions.

2.1 Boundary conditions

Figure 2 shows the schematic diagram of the flow region and the boundary conditions for the present DNS. The inner-to-outer wall radius ratio of the annular channel is $r_i/r_o = 0.5$ and the channel half width is denoted by δ. Only a quarter sector of the full annular cross section is considered in the present study to maintain an adequate grid resolution near the outer wall. The domain size of the inflow generator is chosen as $L/\delta = 5\pi$. For the inflow generator, a grid with 129 × 69 × 129 points is used in the axial, radial and circumferential directions, respectively. The length of the main heated region is $30\pi\delta$, for which a 769 × 69 × 129 grid is used. The adequacy of grid resolution is confirmed with a fine grid solution obtained with twice larger grid points in the radial direction.

The time-dependent inlet velocity profile which is statistically fully-developed is provided by the inflow generator with a periodic condition being imposed in the streamwise direction. The unsteady outlet condition is determined by solving a convection equation for each dependent variable at each time step. The no slip condition is imposed on the wall for each velocity component. The inflow conditions such as the mean velocity and turbulence intensity distributions are verified with the existing DNS results for annular channel flow of Chung *et al.* (2002) and with those of the planar channel flow of Kim *et al.* (1987). As for thermal boundary conditions, the following conditions are imposed at the inlet, inner and outer walls, respectively.

$$h(0,r,\theta;t) = 0, \quad -\frac{k}{c_p}\frac{\partial h}{\partial r}\bigg|_{r=r_i} = Q^+, \quad -\frac{k}{c_p}\frac{\partial h}{\partial r}\bigg|_{r=r_o} = 0. \tag{8}$$

3 SIMULATION CONDITIONS

Table 1 shows the flow conditions considered in the present study. The inlet Reynolds number is Re_0 ($= \rho_0 U_0 D_h/\mu_0 = 4Re$) = 8900 based on the hydraulic diameter ($D_h = 4\delta$) and the inlet bulk velocity (U_0). Three heating conditions of Q^+ = 0.25, 1.20 and 2.40 are investigated at inlet temperature T_0 = 301.15 K. The table also summarizes the buoyancy parameters of the present simulations in terms

Case	Type	Q^+	$\rho_0 U_0$ [kg/m^{2}s]	q_w [kW/m^2]	D_h [mm]	$Gr^*_{D_h}$ ($\times 10^{-8}$)	$\overline{Gr}_b/Re_b^{2.7}$ ($\times 10^4$)	Bo ($\times 10^6$)
C1	CP	0.25	274.62	12.86	2	0	0	0
F1	FC	0.25	274.62	12.86	2	0	0	0
M1	MC	0.25	274.62	12.86	2	0.6997	0.2045	0.8460
C2	CP	1.2	274.62	61.74	2	0	0	0
F2	FC	1.2	274.62	61.74	2	0	0	0
M2	MC	1.2	274.62	61.74	2	3.3584	1.6850	4.0609
C3	CP	2.4	274.62	123.48	2	0	0	0
F3	FC	2.4	274.62	123.48	2	0	0	0
M3	MC	2.4	274.62	123.48	2	6.7167	1.8820	8.1219

Table 1: Summary of the flow conditions for the present DNS. The inlet conditions are the same in all these simulations at $P_0 = 8$ MPa, $T_0 = 301.15$ K, $Re_0 = 8900$ and $Pr_0 = 3.08$. $Gr^*_{D_h}$ and Bo denote the modified Grashof number based on heat flux and the buoyancy parameter, respectively, and both are evaluated at the inlet using the channel hydraulic diameter ($D_h = 4\delta$). $\overline{Gr}_b/Re_b^{2.7}$ is also a commonly used buoyancy parameter whose definition is given in Eq. (11a), and the value shown in the table is the maximum value at each condition. Note that T_{pc} at $P_0 = 8$ MPa is 307.85 K.

of $Gr^*_{D_h}$, $\overline{Gr}_b/Re_b^{2.7}$ and Bo ($= Gr^*_{D_h}/Re_0^{3.425}Pr_0^{0.8}$), where $Gr^*_{D_h}$ ($= 256Gr^*$) and $\overline{Gr}_b$ are the Grashof numbers based on the heat flux and based on the density difference (see Eq. (11a) in Subsection 4.1), respectively. Type CP refers to the constant-property solutions obtained with fluid properties fixed at the inlet values and FC denotes variable-property forced convection without buoyancy effect. Mixed convection with significant buoyancy effects is labeled as MC in the table.

4 RESULTS AND DISCUSSION

In the following discussion, we will omit the superscript * used to denote dimensional quantities for convenience sake and all the results will be presented accordingly.

4.1 Heat transfer characteristics

Nondimensional wall & bulk temperatures and local Nusselt number distributions at the heated inner surface are shown in Figures 3 through 5 for $Q^+ = 0.25$, 1.20 and 2.40, respectively. At each heating condition, the constant-property solution and the variable-property solutions for forced and mixed convections are compared with each other in order to ascertain the effects of strongly-varying properties of supercritical-pressure CO_2 and the buoyancy effect. Also included in the figures are the prediction results from the modified Krasnoschekov & Protopopov correlation (Jackson & Hall, 1979a) and the Dittus-Boelter equation (McAdams, 1942) for fully-established conditions. These correlations are for forced convection heat transfer to supercritical-pressure fluids and are given as follows:

• Modified Krasnoschekov & Protopopov correlation (Jackson & Hall, 1979a);

$$Nu_f = 0.0183 Re_b^{0.82} Pr_b^{0.4} \left(\frac{\rho_w}{\rho_b}\right)^{0.3} \left(\frac{\bar{c}_p}{c_{pb}}\right)^n, \tag{9}$$

where

$$\bar{c}_p = \frac{1}{T_w - T_b}\int_{T_b}^{T_w} c_p dT = \frac{h_w - h_b}{T_w - T_b}.$$

Exponent n in Eq. (9) is not constant and its value depends on the level of T_w and T_b in relation to T_{pc} as follows:

$$n = \begin{cases} 0.4 & \text{for } T_b < T_w \le T_{pc} \text{ or } 1.2T_{pc} \le T_b < T_w, \\ 0.4 + 0.2\left(\frac{T_w}{T_{pc}} - 1\right) & \text{for } T_b \le T_{pc} < T_w, \\ 0.4 + 0.2\left(\frac{T_w}{T_{pc}} - 1\right)\left[1 - 5(\frac{T_b}{T_{pc}} - 1)\right] & \text{for } T_{pc} < T_b \le 1.2T_{pc} \text{ and } T_b < T_w. \end{cases}$$

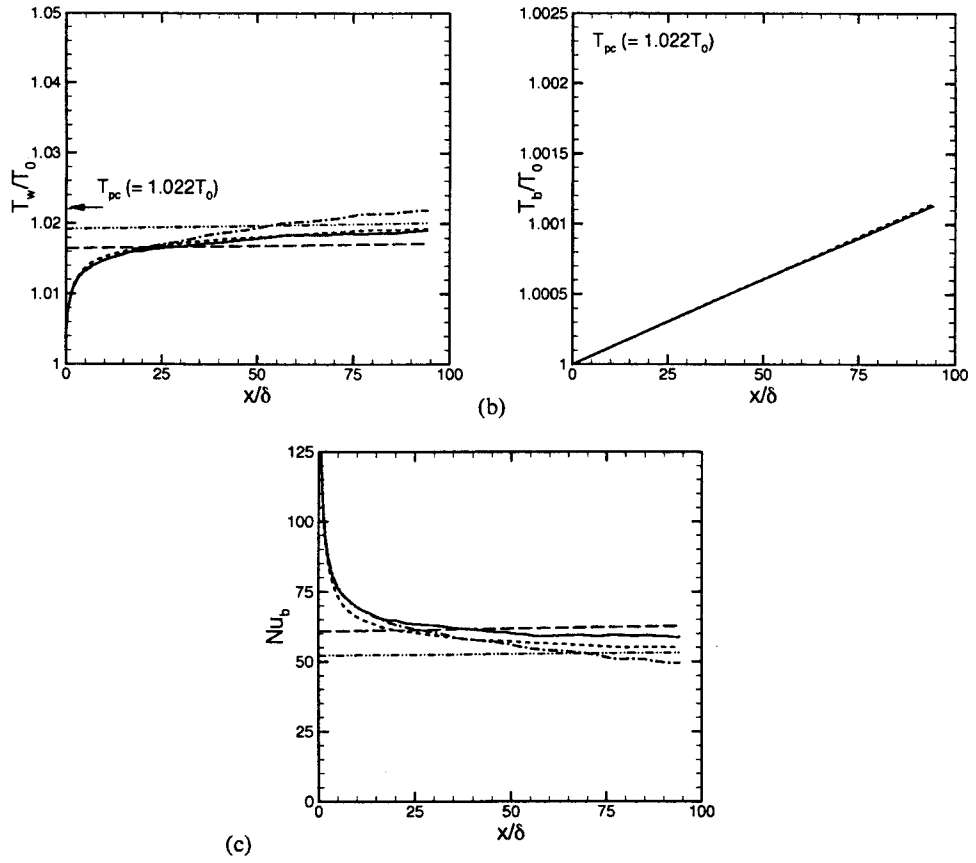

Figure 3: Distributions of nondimensional wall & bulk temperatures and local Nusselt number at the heated inner surface of annulus at $Q^+ = 0.25$: (a) T_w/T_0; (b) T_b/T_0; (c) Nu_b. ·····, Case C1; ———, Case F1; —·—·—, Case M1; — — — (Blue), Modified Krasnoschekov & Protopopov correlation; —··—··— (Red), Dittus-Boelter equation. Empirical correlations are for fully-established flows.

• Dittus-Boelter equation for liquids (McAdams, 1942);

$$Nu_f = 0.023 Re_b^{0.8} Pr_b^{0.4}, \tag{10}$$

where Nu_f denotes the Nusselt number for forced convection and Re_b and Pr_b are the bulk Reynolds and Prandtl numbers evaluated using the properties at local bulk temperature.

As shown in Figure 3, DNS results for cases C1, F1 and M1 are reasonably well matched with the correlations at low Q^+ where the wall-to-bulk temperature difference is very small ($\Delta T = T_w - T_b \approx 6$K) and $T_w < T_{pc}$. The influences of variable-property other than the buoyancy effect are not so significant at this low heating condition, as expected, and a slight increase in Nu_b for case F1 over the results for case C1 is due to a slight reduction in thermal conductivity (k_b) as T_b increases along the flow direction. However, Nu_b for case M1 shows that a measurable reduction (more than 15%) in Nu_b is predicted to occur in the case of mixed convection compared to the buoyancy-free forced convection for case F1, indicating that even at this low heating condition, the buoyancy effect is not negligible. With experimental data for air and water at atmospheric pressure flowing in heated annuli, Jackson (2005) has shown that about a 10% reduction in heat transfer coefficient occurs due to the buoyancy effect at Bo $\approx 5 \times 10^{-7}$, and the present results for case M1 at Bo $= 8.5 \times 10^{-7}$ seem to be very consistent with

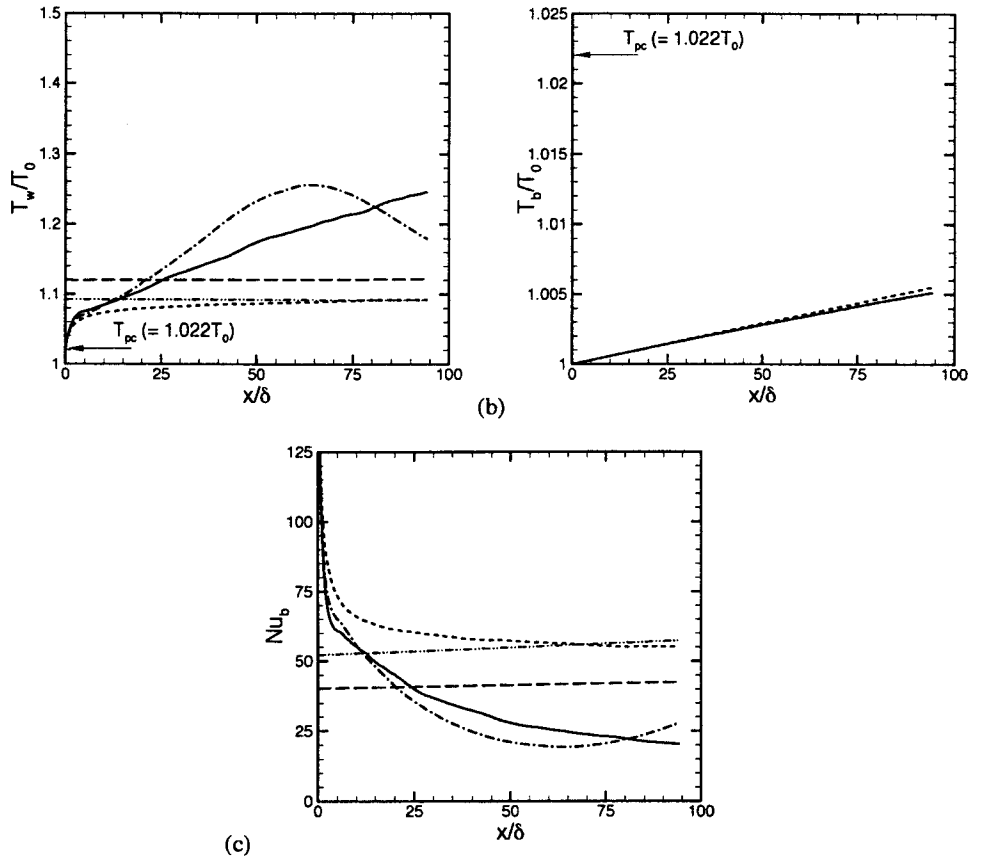

Figure 4: Distributions of nondimensional wall & bulk temperatures and local Nusselt number at the heated inner surface of annulus at $Q^+ = 1.20$: (a) T_w/T_0; (b) T_b/T_0; (c) Nu_b. ·····, Case C2; ——, Case F2; —·—·—, Case M2; – – – – (Blue), Modified Krasnoschekov & Protopopov correlation; —·—·— (Red), Dittus-Boelter equation.

the experimental data.

Figures 4 and 5 show the results for relatively high heating conditions where the imposed heat fluxes are sufficient to produce temperature variations in the fluid which span the whole range of the pseudo-critical region where the $T_b < T_{pc} < T_w$ condition is met. Due to the strong dependence of physical properties on temperature at these conditions, the energy equation becomes highly non-linear so that the proportionality between heat flux and temperature difference no longer exists. With increase in heat flux, the buoyancy effect also increases and the combined effects of these phenomena cause marked differences in heat transfer to supercritical-pressure fluids. As we already mentioned in Section 1, even for forced convection with negligible buoyancy effect, a significant impairment in heat transfer was observed in the experimental data (Shiralkar & Griffith, 1970). Furthermore, none of the existing correlations is known to closely follow these phenomena. As shown in Figure 4(c), even the Krasnoschekov & Protopopov correlation known as the best correlation for forced convection heat transfer to supercritical-pressure fluids overpredicts the heat transfer coefficient significantly, compared to the present results for case F2 or case F3. In fact, these results for cases F2 and F3 at high heating conditions are very similar to those of the experiments of Shiralkar & Griffith (1970). This is clearly demonstrated in the results for case F3 in Figure 5(a) where rather broad peak is observed in the wall temperature distribution near the end.

In the case of mixed convection, however, the results for cases M2 and M3 indicate that the buoyancy

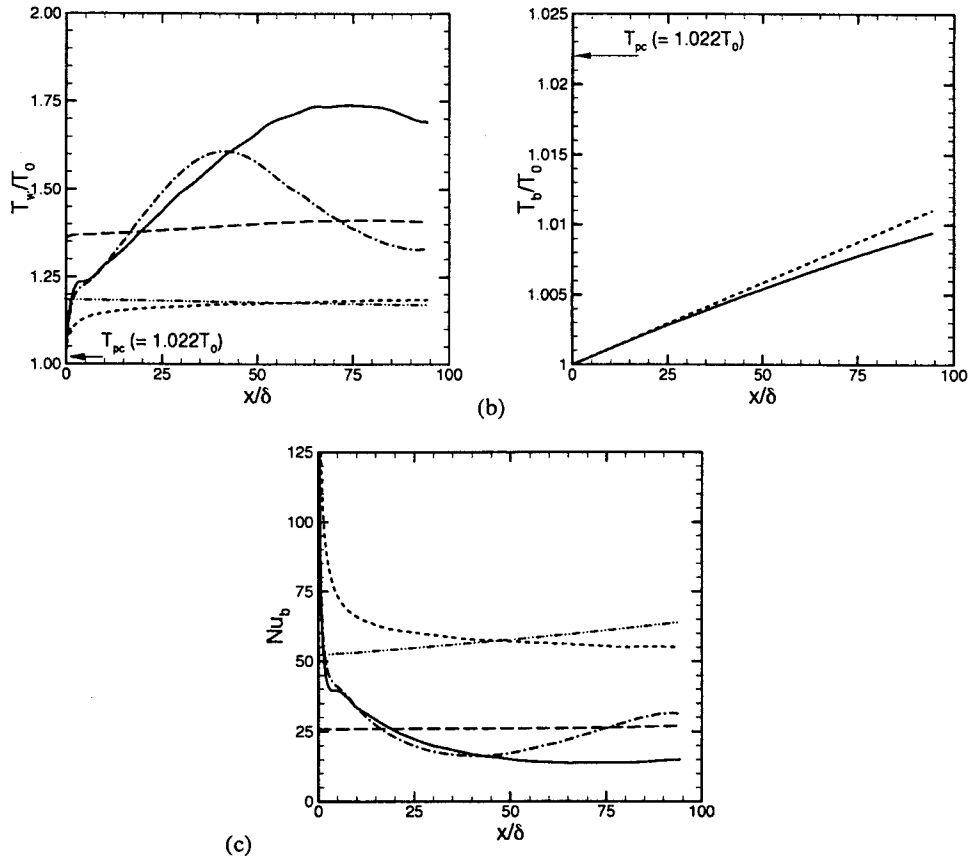

Figure 5: Distributions of nondimensional wall & bulk temperatures and local Nusselt number at the heated inner surface of annulus at $Q^+ = 2.40$: (a) T_w/T_0; (b) T_b/T_0; (c) Nu_b. ·····, Case C3; ———, Case F3; —·—·—, Case M3; – – – – (Blue), Modified Krasnoschekov & Protopopov correlation; —·—·— (Red), Dittus-Boelter equation.

effect causes a rapid rise in wall temperature in the upstream region followed by a large drop after the peak. Consequently, a non-monotonic wall temperature distribution is developed in the axial direction. The wall temperature peak becomes sharper than in the forced convection for case F3, and its axial position moves upstream as the heat flux increases. Before the peak, the heat transfer coefficients for cases M2 and M3 are shown to be lower than for cases F2 and F3, but downstream of the peak the opposite happens so that mixed convection shows a better performance than forced convection. Indeed, these characteristics are very similar in nature to our previous results for supercritical circular pipe flows (Bae *et al.* , 2003) and these results are qualitatively in good agreement with the experimental data (Shitsman (1963); Ackerman (1970); Fewster (1976) etc.) as clearly demonstrated in Figure 6. In Figure 6 the Nusselt number ratios (Nu_b/Nu_f) for mixed convection are plotted in terms of $\overline{Gr}_b/Re_b^{2.7}$ in order to make a direct comparison with the experimental data of Fewster (1976) for upward flows of supercritical-pressure CO_2 in vertical circular tubes. The Grashof number $\overline{Gr}_b$ is based on the density difference as follows:

$$\overline{Gr}_b = \frac{\rho_b - \overline{\rho}}{\rho_b} \frac{gD_h^3}{\nu_b^2}, \qquad \overline{\rho} = \frac{1}{T_w - T_b} \int_{T_b}^{T_w} \rho dT, \tag{11a}$$

where the integrated density $\overline{\rho}$ can be approximated as

$$\overline{\rho} \approx \begin{cases} \frac{1}{2}(\rho_w + \rho_b) & \text{for } T_w < T_{pc} \text{ or } T_b > T_{pc}, \\ \frac{1}{T_w - T_b}\left[\rho_b(T_{pc} - T_b) + \rho_w(T_w - T_{pc})\right] & \text{for } T_b < T_{pc} < T_w. \end{cases} \tag{11b}$$

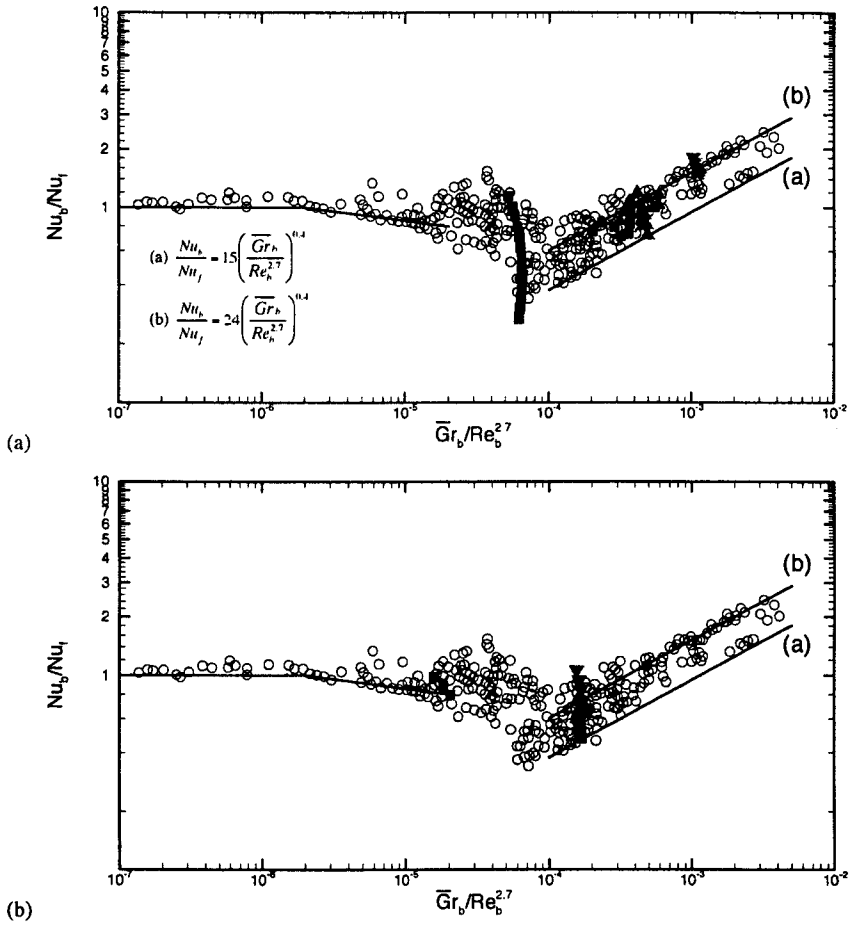

Figure 6: Comparison of Nusselt number ratios between DNS and experiments for upward flow mixed convection of supercritical-pressure CO_2: (a) Circular pipe flows at $Re_0 = 5400$ (Bae *et al.*, 2003); (b) Annular channel flows at $Re_0 = 8900$. Solid symbols, The present DNS; Open symbols, Experimental data of Fewster (1976). The denominator Nu_f is the modified Krasnoschekov & Protopopov correlation given in Eq. (9).

4.2 Mean velocity and shear stress distribution

Figure 7 shows the mean velocity distributions for cases F2 and M2, where the forced and the mixed convection results at $Q^+ = 1.20$ are compared at five locations in the streamwise direction. The profile at $x/\delta = 0$ corresponds to the mean velocity profile for constant-property, fully-developed flow at the inlet. As clearly shown in both subfigures, the local flow acceleration occurs near the heated inner wall in variable-property, supercritical flow due to either thermal expansion or buoyancy effect, both of which are caused by a significant reduction of fluid density. Furthermore, the flow acceleration is considerably larger with buoyancy effects so that the mean velocity profile becomes more asymmetric as the flow progresses downstream (Figure 7(b)).

Along with the changes in the mean velocity profiles, a considerable modification in the shear stress distribution occurs in supercritical flows. In Figure 8, the shear stress distribution is compared at two cross sections for case M2, one is at the inlet ($x/\delta = 0$) and the other is at $x/\delta = 60.44$, farther downstream near the peak wall temperature. As expected from the mean velocity distribution, the mean shear stress profile ($\overline{\tau} = \overline{\mu}/Re(\partial\bar{u}_x/\partial r + \partial\bar{u}_r/\partial x)$) becomes slightly negative at $x/\delta = 60.44$ (Figure 8(b)) with zero crossing point moved much closer to the heated inner wall ($r/\delta = 2.25$). This point may be compared with the radial position of the mean shear stress zero crossing point at the inlet where it

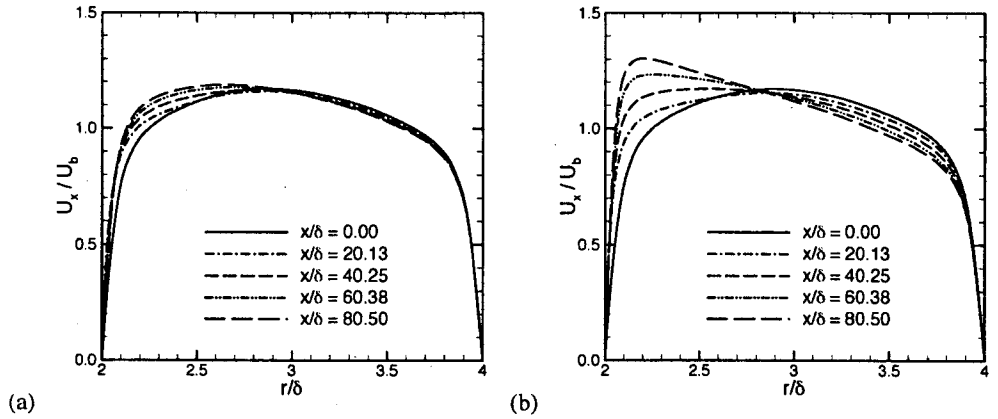

Figure 7: Mean velocity profiles: (a) Case F2, Forced convection; (b) Case M2, Mixed convection. The velocity U_x shown in the figure is the Favre-averaged mean velocity defined as $U_x(=\tilde{u}_x) = \overline{\rho u_x}/\overline{\rho}$.

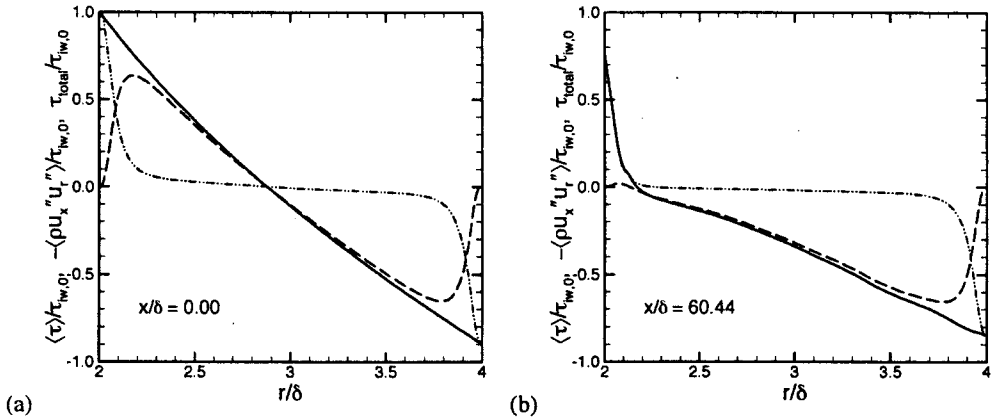

Figure 8: Nondimensional shear stress profiles for case M2: (a) $x/\delta = 0.00$; (b) $x/\delta = 60.44$. Key: $-\cdots-\cdots-$(Red), $\langle\tau\rangle = \bar{\mu}/Re(\partial\bar{u}_x/\partial r + \partial\bar{u}_r/\partial x)$; $-\,-\,-\,-$(Blue), $-\langle\rho u_x'' u_r''\rangle$; ——— (Black), $\tau_{total} = \bar{\mu}/Re(\partial\bar{u}_x/\partial r + \partial\bar{u}_r/\partial x) - \langle\rho u_x'' u_r''\rangle$. Each component of shear stress shown in the figure is normalized with the inner wall shear stress at the inlet ($\tau_{iw,0}$). The velocity $\bar{u}_i$ appearing in the definition of the mean shear stress $\langle\tau\rangle$ is the Reynolds-averaged mean velocity and $-\langle\rho u_x'' u_r''\rangle$ denotes the Reynolds shear stress computed using the Favre averaging.

occurs at $r/\delta = 2.89$ near the center of the channel (Figure 8(a)). However, a much more important change observed at $x/\delta = 60.44$ is the Reynolds shear stress distribution ($-\overline{\rho u_x'' u_r''}$) as shown in Figure 8(b). Compared to the inlet profile for fully-developed turbulent flow, the predicted Reynolds shear stress profile at $x/\delta = 60.44$ is significantly lower, especially near the heated inner wall, so that the negative distribution of the Reynolds shear stress ($-\overline{\rho u_x'' u_r''}$) becomes dominant in the cross section. This fact implies that the buoyancy effect also causes a considerable modification in turbulence as well as in the mean flow field. In Subsection 4.4, we will provide more details on the buoyancy effect on turbulence and will explain how it modifies the transport characteristics of turbulence in supercritical flows.

4.3 Turbulent heat flux distribution

After close examination of various turbulence statistics, we found that the streamwise turbulent heat flux shows a very peculiar behavior in supercritical flows under mixed convection. This is shown in Figure 9 where the results for cases F2 and M2 are presented. Unlike forced convection shown in Figure 9(a), the distribution of streamwise turbulent heat flux ($\overline{\rho u_x'' h''}$) for case M2 shows a very significant variation

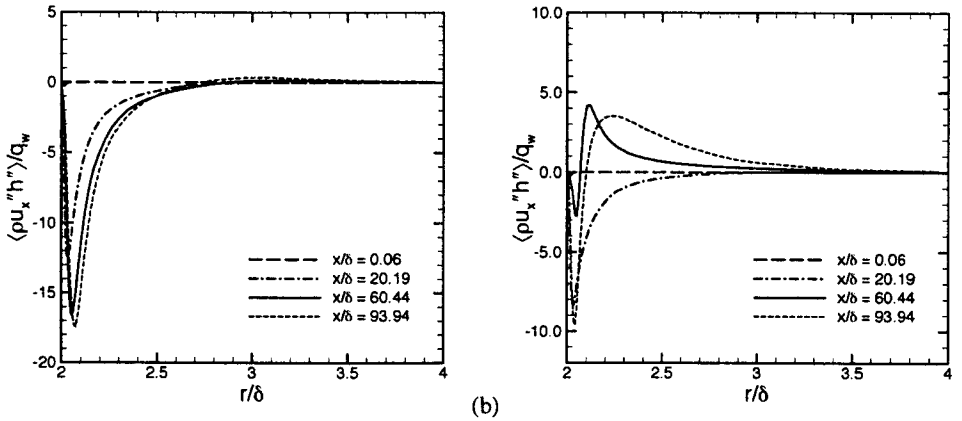

Figure 9: Streamwise turbulent heat flux distributions, $\overline{\rho u_x'' h''}/q_w$: (a) Case F2; (b) Case M2. Note that $\langle \rho u_x'' h'' \rangle$ shown in the ordinate is the same as $\overline{\rho u_x'' h''}$, and the Favre-averaging is used to compute $\overline{\rho u_x'' h''}$ where a double-primed quantity denotes the fluctuations from the Favre-averaged mean value.

along the flow direction, changing both signs and magnitudes. At the upstream region of $x/\delta \leq 20.19$, $\overline{\rho u_x'' h''}$ is first developed in the negative direction, and then its magnitude becomes decreased until x/δ = 60.44 where a positive peak of $\overline{\rho u_x'' h''}$ is observed at $r/\delta \approx 2.1$. Farther downstream, the negative $\overline{\rho u_x'' h''}$ increases again in the negative direction near the heated wall while its positive portion away from the heating surface becomes more widened in the rest of the cross section with slightly reduced peak magnitude. As a consequence of this very unconventional behavior of streamwise turbulent heat flux, mixed convection is subject to a non-monotonic temperature distribution as we have already seen in Figures 4 and 5. However, quite unlike $\overline{\rho u_x'' h''}$, the radial turbulent heat flux ($\overline{\rho u_r'' h''}$) remains *relatively* unchanged with buoyancy effect (although not shown here). This result is because the buoyancy effect is not directly involved in the transport equation for $\overline{\rho u_r'' h''}$ as for the streamwise component. This argument will be made clear in the following subsection.

4.4 Buoyancy effect

The buoyancy effect on turbulence can be best explained via the turbulence transport equations. As explained in the previous subsection, some of the important turbulence statistics change their signs as well as their magnitudes in supercritical flows under strong influence of buoyancy force. Among the Reynolds stress and turbulent heat flux components, only three of them, i.e., $\overline{\rho u_x'' u_x''}$, $\overline{\rho u_x'' u_r''}$ and $\overline{\rho u_x'' h''}$ are directly affected by the gravitational force term in vertical flows so that the buoyancy production terms explicitly appear in the transport equations for $\overline{\rho u_x'' u_x''}$, $\overline{\rho u_x'' u_r''}$ and $\overline{\rho u_x'' h''}$. In order to show this, let us focus on the gravitational force term when we derive the transport equation. As an example, consider that the transport equation for $\overline{\rho u_x'' u_x''}$ is derived as follows:

$$\bar{\rho}\frac{\mathrm{D}(\widetilde{u_x'' u_x''})}{\mathrm{D}t} = \left[\frac{\partial}{\partial t}(\overline{\rho u_x'' u_x''}) + \frac{\partial}{\partial x_j}(\tilde{u}_j \overline{\rho u_x'' u_x''})\right] = \ldots - 2\overline{u_x''}\frac{\partial \bar{p}}{\partial x}, \tag{12}$$

where the gravitational force is included in terms of the mean pressure gradient along the axial direction; $\partial \bar{p}/\partial x$ is determined from the mean momentum equations,

$$-\frac{\partial \bar{p}}{\partial x_i} = \frac{\partial}{\partial x_j}(\bar{\rho}\tilde{u}_j\tilde{u}_i) - \frac{\partial}{\partial x_j}(\bar{\tau}_{ij} - \overline{\rho u_i'' u_j''}) + \frac{g\delta}{U_0^2}\delta_{i1}\bar{\rho}. \tag{13}$$

Then, Eq. (12) becomes

$$\bar{\rho}\frac{\mathrm{D}(\widetilde{u_x''u_x''})}{\mathrm{D}t} = \ldots - 2\overline{u_x''}\frac{\partial \bar{p}}{\partial x} = \ldots + 2\frac{g\delta}{U_0^2}\bar{\rho}\overline{u_x''}$$
$$= \ldots - 2\frac{g\delta}{U_0^2}\overline{\rho' u_x'}, \tag{14}$$

where $\overline{u_x''}$ is replaced by $-\overline{\rho' u_x'}/\bar{\rho}$ in the last equality. Similarly, the transport equations for $\overline{\rho u_x'' u_r''}$ and $\overline{\rho u_x'' h''}$ can be obtained as follows:

$$\bar{\rho}\frac{\mathrm{D}(\widetilde{u_x''u_r''})}{\mathrm{D}t} = \ldots - \frac{g\delta}{U_0^2}\overline{\rho' u_r'}, \tag{15}$$

$$\bar{\rho}\frac{\mathrm{D}(\widetilde{u_x''h''})}{\mathrm{D}t} = \ldots - \frac{g\delta}{U_0^2}\overline{\rho' h'}. \tag{16}$$

where single- and double-primed quantities denote the fluctuations from the Reynolds- and Favre-averaged mean values, respectively. A Favre-averaged mean, $\tilde{\phi}$, is defined as $\tilde{\phi} = \overline{\rho\phi}/\bar{\rho}$.

As shown in the above equations, three kinds of buoyancy production terms arise from the correlations of $\overline{\rho' u_x'}$, $\overline{\rho' u_r'}$ and $\overline{\rho' h'}$ all of which turned out to be non-negligible in supercritical flows where density change is very significant, especially near the pseudo-critical region. This fact is quite different from the ideal gas flows where these correlations except $\overline{\rho' u_r'}$ are typically neglected under the assumption of the Morkovin's hypothesis (Morkovin, 1961).

Very interestingly, the radial profiles of $-2(g\delta/U_0^2)\overline{\rho' u_x'}$ shown in Figure 10(a) are strikingly similar to those of $\overline{\rho u_x'' h''}$ (see Figure 9(b)). However, this is not coincidental because the correlations $-\overline{\rho' u_x'}$ and $\overline{u_x' h'}$ (which determine $\overline{\rho u_x'' h''}$ primarily when multiplied by the mean density, $\bar{\rho}$) are always of the same sign since ρ' and h' should be negatively correlated at all times. Therefore, $\overline{\rho u_x'' h''}$ and the buoyancy production term $-2(g\delta/U_0^2)\overline{\rho' u_x'}$ for the Reynolds normal stress should have nearly identical distributions. Furthermore, the effect of the positive contribution of $-(g\delta/U_0^2)\overline{\rho' h'}$ to $\overline{\rho u_x'' h''}$ shown in Figure 10(c) also causes $\overline{\rho u_x'' h''}$ to develop into the positive direction although its effect is not as significant as that of $\overline{u_x' h'}$ or $-\overline{\rho' u_x'}$. These two reasons explain why the streamwise turbulent heat flux shows such an unique behavior in upward supercritical flows. In the meanwhile, Figure 10(b) shows that the effects of $-(g\delta/U_0^2)\overline{\rho' u_r'}$ on $\overline{\rho u_x'' u_r''}$ are overall positive so that the Reynolds shear stress $(-\overline{\rho u_x'' u_r''})$ should decrease near the heated inner wall as we have already shown in Figure 8(b).

With the same reasoning, it is now easy to understand that the buoyancy effect on turbulence kinetic energy, $k(= 1/2\overline{\rho u_i'' u_i''}/\bar{\rho})$, which is most frequently discussed to explain the physical mechanism of heat transfer deterioration phenomena, is determined by the term $-(g\delta/U_0^2)\overline{\rho' u_x'}$ which is a half of those shown in Figure 10(a). Because of this term, the turbulence kinetic energy per unit volume begins to increase again across the cross section at $x/\delta = 60.44$ where the predicted turbulence kinetic energy shows a minimum near the heated wall as shown in Figure 11(b). This explains why the buoyancy effect often shows two completely different aspects on turbulence in upward flows, i.e., attenuation and enhancement.

4.5 Instantaneous flow field

In Figures 12 and 13, instantaneous flow fields for case M3 are investigated at two cross sections. The first one is at $x/\delta = 35.77$ near which a local maximum wall temperature is observed (see Figure 5) and the second is at $x/\delta = 85.11$ near the end of the computational domain where the wall temperature subsides substantially. The local density distribution (represented by color-flooded contours), overlapped with its fluctuation contours (represented by line contours), is shown in Figure 12 while Figure 13 shows the streamwise velocity component. As shown in Figure 12, local density variations are significant

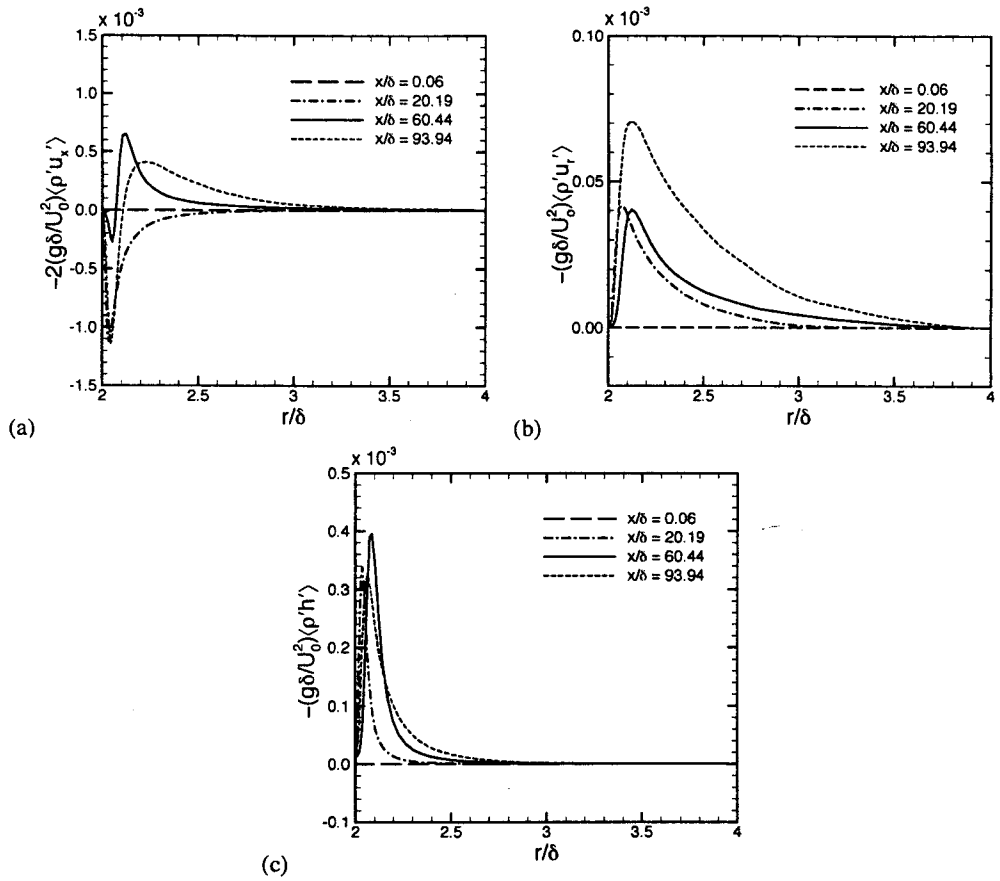

Figure 10: Buoyancy production terms for case M2: (a) $-2(g\delta/U_0^2)\langle\rho' u_x'\rangle$; (b) $-(g\delta/U_0^2)\langle\rho' u_r'\rangle$; (c) $-(g\delta/U_0^2)\langle\rho' h'\rangle$

near the heating surface but an almost uniform distribution is observed near the adiabatic outer wall. Fluctuation contours indicate that the low density layer near the heating surface at $x/\delta = 35.77$ is quite stable with low level of fluctuations (Figure 12 (a)) but no similar stable density layer is found at $x/\delta = 85.11$ where substantially larger density fluctuations are developed (Figure 12 (b)). Instantaneous velocity distributions are also very different between these two cross sections. With flow acceleration due to buoyancy forces, high velocity regions are more frequently found near the heating surface at $x/\delta = 85.11$ as indicated by colored regions in Figure 13(b). Velocity fluctuations are also substantially increased at $x/\delta = 85.11$. As we already examined in subsection 4.4, the buoyancy effect causes a complicated modification in turbulence, and Figure 13 clearly shows the results of turbulence attenuation and enhancement due to buoyancy effect at $x/\delta = 35.77$ and $x/\delta = 85.11$, respectively.

5 CONCLUSIONS

A series of direct numerical simulations was performed for upward flows in a vertical annular channel using supercritical-pressure CO_2 to investigate variable-property effects on turbulent convective heat transfer. The present study is concerned with thermally-developing flows of supercritical-pressure fluids in a heated annulus where the inner wall is heated with constant heat flux and an adiabatic condition is imposed on the outer wall. The inlet Reynolds number based on the channel hydraulic diameter and the bulk velocity is $Re_0 = 8900$. Variable-property effects of supercritical-pressure fluid are shown to be very significant in terms of integral wall parameters and mean velocity/shear stress distributions as well as tur-

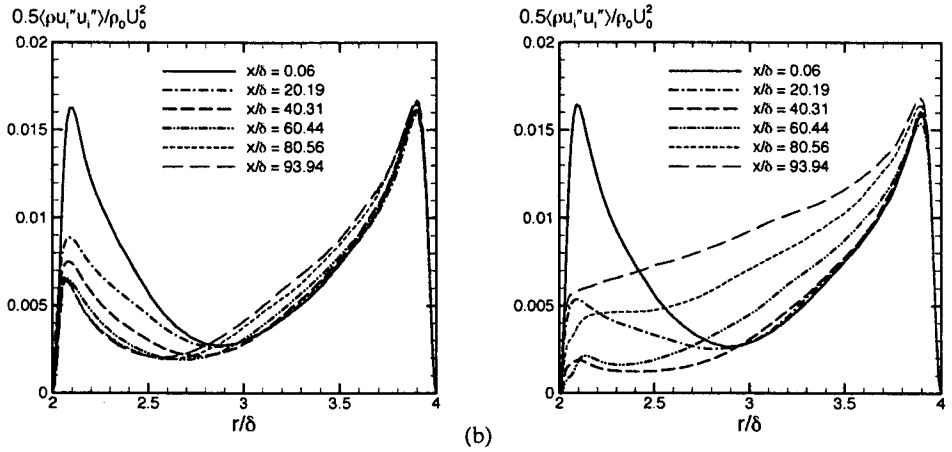

Figure 11: Turbulence kinetic energy distributions, $(1/2)\overline{\rho u_i'' u_i''}/\rho_0 U_0^2$: (a) Case F2; (b) Case M2. Note that $\langle \rho u_i'' u_i'' \rangle$ shown in the ordinate is the same as $\rho u_i'' u_i''$ where $\overline{\rho u_i'' u_i''} = \overline{\rho u_x'' u_x''} + \overline{\rho u_r'' u_r''} + \overline{\rho u_t'' u_t''}$.

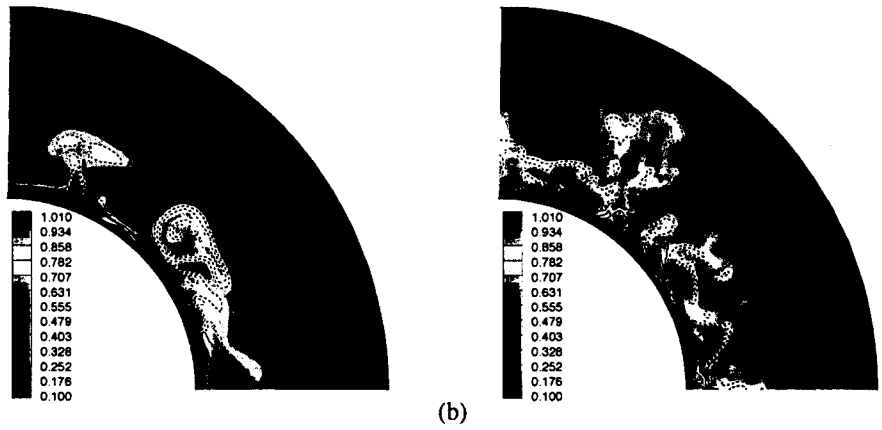

Figure 12: Instantaneous density distribution for case M3: (a) $x/\delta = 35.77$; (b) $x/\delta = 85.11$. Key: color-flooded contours, ρ/ρ_0; line contours, $-0.5 \leq \rho'/\rho_b \leq 0.4$ with increment of 0.075. Negative fluctuations are drawn with dashed lines. Note that density ratio at the pseudo-critical temperature is $\rho_{pc}/\rho_0 = 0.6286$ for this condition.

bulence statistics, so that the characteristics of turbulent convective heat transfer to supercritical-pressure fluid become very different from those of the constant-property flow. Significant density reduction causes the mean velocity profile to be locally accelerated near the heated wall due to the buoyancy effect, which changes the shear stress distribution considerably. It is also shown that the effect of temporal density fluctuations is particulary important in supercritical flows, changing turbulence transport characteristics significantly via the buoyancy production terms arising from the correlations such as $\overline{\rho' u_x'}$, $\overline{\rho' u_r'}$ and $\overline{\rho' h'}$. Among various turbulence statistics, the streamwise turbulent heat flux shows a very peculiar transitional behavior with buoyancy effect, changing both in sign and magnitude. Consequently, a non-monotonic temperature distribution is developed along the flow direction, which causes severe impairment of heat transfer in supercritical flows.

6 ACKNOWLEDGEMENTS

This work has been conducted under a joint RoK/US I-NERI Project, and the Creative Research Initiative (CRI), both under the auspices of the Korea Institute of Science and Technology Evaluation and Planning (KISTEP).

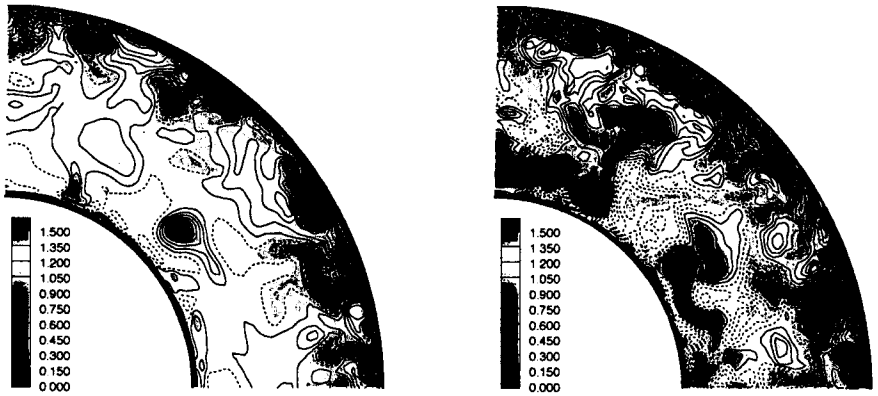

Figure 13: Instantaneous streamwise velocity distribution for case M3: (a) $x/\delta = 35.77$; (b) $x/\delta = 85.11$. Key: color-flooded contours, u_x/U_0; line contours, $-0.5 \leq u'_x/U_b \leq 0.5$ with increment of 0.05. Negative fluctuations are drawn with dashed lines.

REFERENCES

Ackerman, J. W. 1970. Pseudoboiling heat transfer to supercritical pressure water in smooth and ribbed tubes. *J. Heat Transfer, Trans. ASME*, **92**, 490–498.

Bae, J. H., Yoo, J. Y., & Choi, H. 2003. Direct numerical simulation of heat transfer to CO_2 at supercritical pressure in a vertical tube. *In: Proceedings of the Tenth International Topical Meeting on Nuclear Reactor Thermal Hydraulics (NURETH-10), Paper No. A00114, October 5-11, Seoul, Korea.*

Cheng, X., Schulenberg, T., Bittermann, D., & Rau, P. 2003. Design analysis of core assemblies for supercritical pressure conditions. *Nuclear Engineering and Design*, **223**, 279–294.

Chung, S. Y., Rhee, G. H., & Sung, H. J. 2002. Direct numerical simulation of turbulent concentric annular pipe flow, Part 1: Flow Field. *Int. J. Heat Fluid Flow*, **23**, 426–440.

Duffey, R. B., & Pioro, I. L. 2005. Experimental heat transfer of supercritical carbon dioxide flowing inside channels (survey). *Nuclear Engineering and Design*, **235**, 913–924.

Fewster, J. 1976. *Mixed, forced and free convective heat transfer to supercritical pressure fluids flowing in vertical pipes.* Ph.D. thesis, University of Manchester.

He, S., Kim, W. S., Jiang, P. X., & Jackson, J. D. 2004. Simulation of mixed convection heat transfer to carbon dioxide at supercritical pressure. *J. Mech. Engrg. Sci.*, **218**, 1281–1296.

Jackson, J. D. 2005. Private communication, University of Manchester.

Jackson, J. D., & Hall, W. B. 1979a. Forced convection heat transfer to fluids at supercritical pressure. *Pages 563–611 of:* Kakac, S., & Spalding, D. B. (eds), *Turbulent forced convection in channels and bundles*, vol. 2. Hemisphere Publishing Corporation.

Jackson, J. D., & Hall, W. B. 1979b. Influences of buoyancy on heat transfer to fluids flowing in vertical tubes under turbulent conditions. *Pages 613–640 of:* Kakac, S., & Spalding, D. B. (eds), *Turbulent forced convection in channels and bundles*, vol. 2. Hemisphere Publishing Corporation.

Kim, J., Moin, P., & Moser, R. 1987. Turbulence statistics in fully developed channel flow at low Reynolds number. *J. Fluid Mech.*, **177**, 133–166.

Koshizuka, S., Takano, N., & Oka, Y. 1995. Numerical analysis of deterioration phenomena in heat transfer to supercritical water. *Int. J. Heat Mass Transfer*, **38**, 3077–3084.

McAdams, W. H. 1942. *Heat Transmission.* 2nd edn. New York: McGraw-Hill.

McCreery, G. E., Pink, R. J., Condie, K. G., & McEligot, D. M. 2003. Fluid dynamics of ribbed annuli. *In: Proceedings of the Tenth International Topical Meeting on Nuclear Reactor Thermal Hydraulics (NURETH-10), Paper No. J00203, October 5-11, Seoul, Korea.*

McEligot, D. M., & Jackson, J. D. 2004. Deterioration criteria for convective heat transfer in gas flow through non-circular ducts. *Nuclear Engineering and Design*, **232**, 327–333.

Morkovin, M. V. 1961. Effects of compressibility on turbulent flows. *Pages 367–380 of:* Favre, A. (ed), *Mechanique de la Turbulence.* Paris, France: Centre National de la Recherche Scientific.

Pierce, C. D. 2001. *Progress-variable approach for large-eddy simulation of turbulent combustion.* Ph.D. thesis, Stanford University.

Pierce, C. D., & Moin, P. 2004. Progress-variable approach for large-eddy simulation of non-premixed turbulent combustion. *J. Fluid Mech.*, **504**, 73–97.

Pioro, I. L., Khartabil, H. F., & Duffey, R. B. 2004a. Heat transfer to supercritical fluids flowing in channels - empirical correlations (survey). *Nuclear Engineering and Design*, **230**, 69–91.

Pioro, I. L., Duffey, R. B., & Dumouchel, T. J. 2004b. Hydraulic resistance of fluids flowing in channels at supercritical pressures (survey). *Nuclear Engineering and Design*, **231**, 187–197.

PROPATH Group. 1999. *PROPATH: A Program Package for Thermophysical Properties of fluids, Ver. 11.1.* The International Association for the Properties of Water and Steam (IAPWS), http://www.iapws.org.

Shiralkar, B. S., & Griffith, P. 1970. The effect of swirl, inlet conditions, flow direction, and tube diameter on the heat transfer to fluids at supercritical pressure. *J. Heat Transfer, Trans. ASME*, **92**(3), 465–474.

Shitsman, M. E. 1963. Impairment of heat transmission at supercritical pressures. *High Temperature*, **1**(2), 237–244.

Sonntag, R. E., & Van Wylen, G. J. 1981. *Introduction to Thermodynamics, Classical and Statistical.* 2nd edn. John Wiley & Sons. Chap. 3, pages 37–43.

Wall, C., Pierce, C. D., & Moin, P. 2002. A semi-implicit method for resolution of acoustic waves in low Mach number flows. *J. Comput. Phys.*, **181**, 545–563.